inorganics

MDPI

Article

Two Mechanism Pathways from a Versatile Arene Ruthenium Assembly: Reaching Aqueous Sensing Reversibility and Selectivity for CN^-

Alaa Maatouk [1], Thibaud Rossel [1], Gioele Colombo [2], Stefano Brenna [2] and Bruno Therrien [1,*]

[1] Institute of Chemistry, University of Neuchatel, Ave. de Bellevaux 51, CH-2000 Neuchatel, Switzerland
[2] Department of Science and High Technology, University of Insubria, Via Valleggio 9, 22100 Como, Italy; gioele.colombo@uninsubria.it (G.C.); stefano.brenna@uninsubria.it (S.B.)
* Correspondence: bruno.therrien@unine.ch

Abstract

The development of highly selective, sensitive and recyclable chemosensors for CN^- is critical due to the widespread use of cyanide derivatives in industrial processes and its extreme toxicity to environmental and biological systems. Herein, we report the synthesis and characterization of a water-soluble arene ruthenium metalla-assembly specifically designed to operate in aqueous solutions and under environmentally relevant conditions. The arene ruthenium assembly incorporates functionalized building blocks that enable a selective multi-site recognition of cyanide according to pH by either nucleophilic addition or hydrogen bond interactions. The system exhibits a distinct colorimetric response upon cyanide binding, resulting in a rapid "turn-on" color change. An excellent selectivity and reversibility for cyanide recognition is observed over multiple cycles, with a detection limit in the low micromolar range, thus laying the ground for the future development of sensing technology with supramolecular metal-based assemblies.

Keywords: arene ruthenium; coordination-driven self-assembly; regenerable sensor; cyanide detection; nucleophilic addition; ruthenium-based sensor

Academic Editors: Wanhe Wang, Jing Wang and Xiao Yao

Received: 26 September 2025
Revised: 22 October 2025
Accepted: 25 October 2025
Published: 28 October 2025

Citation: Maatouk, A.; Rossel, T.; Colombo, G.; Brenna, S.; Therrien, B. Two Mechanism Pathways from a Versatile Arene Ruthenium Assembly: Reaching Aqueous Sensing Reversibility and Selectivity for CN^-. *Inorganics* **2025**, *13*, 357. https://doi.org/10.3390/inorganics13110357

1. Introduction

Cyanide (CN^-) is a highly toxic anion for most organisms, showing potent inhibitory effects on essential cellular enzymes, particularly cytochrome c oxidase [1,2]. Exposure to cyanide, even at trace levels, can disrupt cellular respiration and lead to severe physiological damage or death [3]. Despite their high toxicity, cyanides are extensively used in industries, including mining, electroplating and chemistry, making their presence in the environment a significant concern [3]. Therefore, the development of rapid, selective and sensitive detection methods for cyanide is of the utmost importance for environmental monitoring, industrial safety and forensic analysis [4].

In this context, the World Health Organization sets the maximum permissible level of cyanide in water at a concentration of 1.9 μM [5,6]. Traditional methods for cyanide detection, including titrimetric, electrochemical and spectroscopic techniques, often require sophisticated instrumentations and can suffer from time-consuming sample preparation [7]. As a strategy, chemosensing, which relies on the interaction between a molecular receptor and a targeted analyte to produce a measurable signal, has emerged as a promising approach for cyanide monitoring [8,9].

Chemosensors offer several advantages, including simplicity, real-time detection and the potential for high selectivity and sensitivity, thanks to molecular design. Recent advances in fluorometric and colorimetric chemosensors for the detection of cyanide have led to the innovation of a diverse range of optical probes. These include small organic molecules functionalized with selective recognition units such as boronic acid [10], organoborane [11], thiourea [12], imidazolium [13], oxazine [14], porphyrin [15] and dicyanovinyl [16], each improving sensitivity and/or selectivity. In addition, advances in metal-based probes [17,18], polymer frameworks [19] and nanoparticle-integrated sensors [20], have expanded the scope of detection strategies, exploiting structural aspects and mechanistic attributes to improve analytical response.

The detection of cyanide via optical probes predominantly relies on two approaches. The reaction-dependent strategy is the most widely employed. This approach exploits the strong nucleophilicity of CN^-, targeting electrophilic sites, thus shifting the equilibrium to cyanide adducts that produce measurable optical responses. The mechanisms can be based on nucleophilic addition to aldehydes or ketones [21], Michael addition [22,23], cyanide-induced cleavage reactions of spirocyclic compounds [24], cyanide-induced decomplexation reactions [25] or cyanide-induced cyclization reactions in imine-based sensors [26]. However, such sensors predominantly operate in organic or mixed solvents, as the strong solvation of CN^- in water decreases its reactivity with carbonyl groups and limits their applicability in aqueous media. In addition, a lack of reversibility and a dependence on external energy input result in slow responsive times, reducing attractiveness.

The second strategy involves weaker interactions, where CN^- binds to hydrogen bond receptors to induce supramolecular optical changes [27–29]. Again, under physiological conditions, the CN^- tends to be surrounded by water molecules, thus weakening its interaction with hydrogen bond donors and restricting the sensor's applicability for biological systems [30]. Nevertheless, CN^- remains a strong base in water, meaning that adjusting the acidity of the donor and the working pH can increase selectivity. Therefore, incorporating electron-withdrawing groups or metal centers to enhance the hydrogen acidity of a sensor are effective strategies to increase selectivity and sensitivity to CN^- detection in protic solvents [31].

In this regard, cationic Ru(II)–polypyridyl complexes have been effectively used as chemosensors due to their remarkable luminescent properties [32], which make them highly suitable for sensing [33]. Indeed, several mono and bimetallic Ru(II) probes consisting of racemic mixtures of Δ- and Λ-isomers have been developed for CN^- sensing. For example, Li et al. [34] and Yao et al. [35] have developed Ru(II) complexes with carboxaldehyde-functionalized ligands, which exploit a nucleophilic attack of CN^- on an aldehyde (Figure 1a), leading to the formation of cyanohydrin and to luminescent changes. Furthermore, a series of Ru(II) complexes featuring imidazole-functionalized ligands have been developed as an advanced strategy for CN^- sensing (Figure 1b) [36–39]. In these systems, the Ru(II) center plays a crucial role in the detection mechanism, as it facilitates ligand preorganization by optimally positioning the hydrogen bond donor groups and also enhances the hydrogen bond acidity, thus increasing the binding affinity for CN^- and triggering a luminescence response.

Although significant progress has been made in optical cyanide sensing, several obstacles remain, including intricate synthetic procedures, limited water solubility and insufficient selectivity in aqueous media. Furthermore, challenges such as sensor instability and decreased efficiency due to an elevated limit of detection (LOD) in protic media continue to hinder performances and applicabilities [40–42]. Therefore, designing simple, affordable, and highly selective and sensitive probes for cyanide detection is crucial, but remains a difficult task.

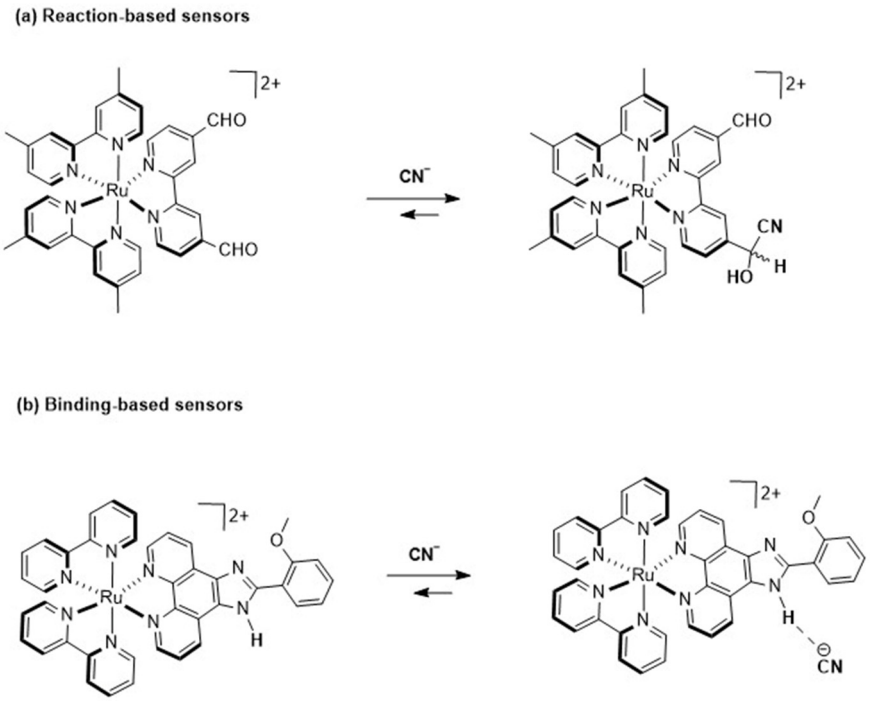

Figure 1. Two ruthenium(II)–polypyridyl complexes used as optical CN^- sensors: (**a**) reaction-dependent strategy; (**b**) hydrogen bond strategy.

In recent years, metalla-assemblies have attracted considerable attention as chemical sensors [43–49], due to their well-defined geometries, tunable structural sizes and inherent stability in various media [50]. Their straightforward synthesis and structural versatility, combined with functionalized molecular components, allow selective recognition of diverse analytes. Among them, arene ruthenium metalla-rectangles represent a promising class of supramolecular architectures for sensing. These complexes exhibit exceptional stability in aqueous environments, with host–guest interactions typically governed by mechanisms such as nucleophilic addition, hydrogen bonding, π–π staking or complexation, leading to detectable photophysical changes [51,52]. Recent advancement in arene ruthenium metalla-rectangles have facilitated the development of sophisticated sensing platforms, expanding their applicability, especially in aqueous media [53].

To the best of our knowledge, no metalla-rectangle or coordination cages have been reported for the selective naked-eye detection of cyanide in water. Herein, we have developed the first arene ruthenium metalla-rectangle for cyanide detection employing a dual sensing mechanism that demonstrates high selectivity, sensitivity, reversibility and a fast response under environmentally relevant conditions. This work not only contributes to the growing field of anion sensing but also addresses the urgent need for effective water-compatible cyanide detection strategies in industrial and environmental contexts.

2. Results

Synthesis and characterization of MRDPP: An arene ruthenium metalla-assembly incorporating diketopyrrolopyrrole (DPP) was successfully synthesized in methanol at room temperature. As illustrated in Scheme 1, the reaction consisted of mixing the dinuclear complex [{Ru(*p*-cymene)}$_2$bis(2-hydroxyethyl)ethanediamide}Cl_2] with silver triflate in the presence of 3,6-di(pyridin-4-yl)-2,5-dihydropyrrolo [3,4-*c*]pyrrole-1,4-dione to form the tetracationic complex [{Ru(*p*-cymene)}$_4$bis(2-hydroxyethyl)ethanediamide}$_2$3,6-di(pyridin-4-yl)-2,5-dihydropyrrolo [3,4-*c*]pyrrole-1,4-dione}$_2$]$^{4+}$ (MRDPP), which was iso-

lated in an excellent yield (98%) as its triflate salt. The MRDPP complex significantly increases the solubility of the DPP moiety, which on its own is almost insoluble [54].

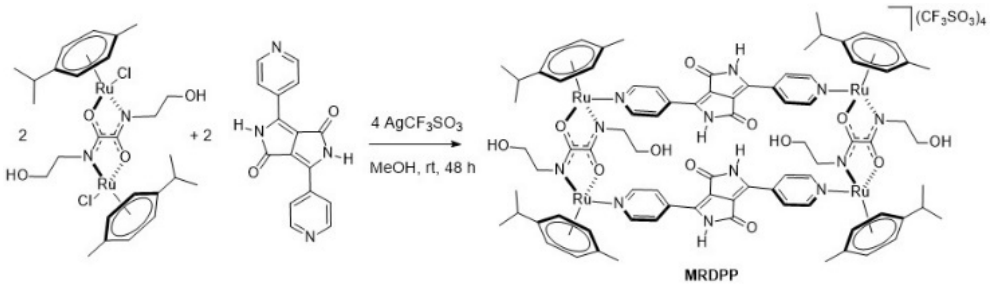

Scheme 1. Synthesis of metalla-rectangle MRDPP.

The molecular structure was characterized by ^{1}H, ^{13}C NMR, DOSY (Diffusion Ordered SpectroscopY), UV-vis (Figure 2) and mass spectrometry (Figures S1–S4). MRDPP is highly soluble in common organic solvents, including methanol, ethanol, dimethyl sulfoxide and acetonitrile. Like other compounds containing the DPP chromophore moiety [54], MRDPP exhibits an intense coloration with solvent-dependent UV-vis absorption bands in the range of 450 to 700 nm (Figure 2). This optical behavior originates from a combination of $\pi \rightarrow \pi^*$ transitions, made possible by the extended π conjugation of the DPP core and metal–ligand charge transfer transitions (MLCT: $d_{\mathrm{Ru\ (II)}} \rightarrow \pi^*_{\mathrm{DPP}}$) from the Ru(II) centers to the π-acceptor DPP unit [55]. The absorption spectra show pronounced solvatochromic effects, reflecting the high sensitivity of these electronic transitions to the dielectric constant and the polarity of the surrounding solvent. In polar protic solvents such as ethanol, methanol and water, an improved ligand-centered LUMO stabilization reduces the HOMO-LUMO energy gap, resulting in a bathochromic-shifted absorption band. On the other hand, aprotic polar solvents such as acetonitrile provide fewer hydrogen bond interactions, leading to a sharper and more defined absorption band centered at ≈540 nm. The chromophore shows high absorption in acetonitrile, with an extinction coefficient (ε) of 1.6×10^4 L·mol^{-1}·cm^{-1} and low absorbance in ethanol (ε = 0.6×10^4 L·mol^{-1}·cm^{-1}), while in water the ε is 1.08×10^4 L·mol^{-1}·cm^{-1}, indicating moderate molar absorptivity.

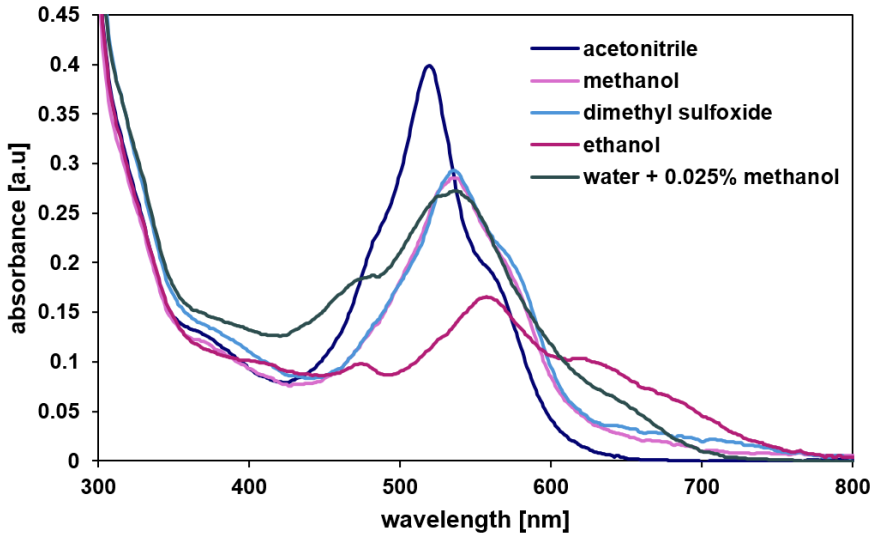

Figure 2. UV-vis absorption spectra of MRDPP in various solvents.

It should be noted that the DPP moiety on the panels of the MRDPP metalla-rectangle have two possible conformational arrangements, one favoring intramolecular interactions between lactam groups with limited π-π stacking (anti-isomer), while the other shows

strong π-π stacking interactions between the DPP units (syn-isomer) (Figure S5). These different conformations and the stereogenic nature of the ruthenium centers complicate the ^{1}H NMR spectrum of MRDPP (Figure S1) by reducing the symmetry and making broad and poorly defined signals. However, the DOSY NMR spectrum shows the presence of a single alignment of the signals (Figure S3), suggesting the formation of single-sized assemblies, which is consistent with the proposed structures. The anti- and syn-MRDPP conformations (Figure S5) have a similar hydrodynamic radius, thus leading to the same diffusion coefficient and accordingly appearing as a single signal in the DOSY spectrum. Furthermore, two characteristic peaks in the ESI-MS spectrum can be observed, both being attributed to the intact MRDPP cation after the loss of triflate anions: $[MRDPP–3CF_3SO_3]^{3+}$ (m/z = 673.43) and $[MRDPP–4CF_3SO_3]^{4+}$ (m/z = 467.58) (Figure S4).

Naked-eye recognition of anions by MRDPP in various solvents: To study the solvent-dependent colorimetric sensing behavior of MRDPP, qualitative visual recognition experiments were conducted in acetonitrile, ethanol and distilled water (+0.025% v/v methanol) with the following anions: CN^-, SCN^-, F^-, Cl^-, Br^-, I^-, IO_3^-, PO_4^{3-}, CO_3^{2-}, NO_3^-, $CH_3CO_2^-$, SO_4^{2-}, SO_3^{2-} and $C_6H_5O_7^{3-}$ (citrate). Anions were introduced at a 1 mM (40 eq.) concentration in the presence of MRDPP (25 μM, 1 eq.). The results revealed a strong effect of solvent on the response. As can be observed in Figure 3, MRDPP shows distinct solvent colors dependence: dark pink in water, bright pink in acetonitrile and bluish gray in ethanol. Upon CN^- addition, clear and solvent-driven color changes can be observed, allowing selective naked-eye detection. In distilled water, the solution turned gray; this attenuated color suggests a limited host–guest interaction, probably due to the strong solvation and hydrogen bonding competition. In contrast, a stunning pink-to-green shift can be observed in acetonitrile, suggesting a strong interaction between MRDPP and CN^-, facilitated by the aprotic nature of the solvent [40,56]. Ethanol produced a green–blue shift, distinct from that in acetonitrile, possibly due to the partial contribution of the solvent for hydrogen bonds. Interestingly, other anions do not initiate color changes in water and ethanol. However, the loss of a large portion of the solvation energy for PO_4^{3-} and CO_3^{2-}, when moving from water and ethanol to acetonitrile, improves their interactions with MRDPP, which also turns the solution green. Nevertheless, the strong and selective visual response towards cyanide remains dominant in water, highlighting the capacity of MRDPP to act as a selective colorimetric chemosensor for cyanide.

Hydrogen bond cleavage-driven cyanide sensing in distilled water: UV–visible absorption was measured to confirm the visual effects of the initial experiments and to gain further insights into the recognition capacity of the probe towards anions in aqueous media. In this series of anions, the selection of biodegradable citrate is not related to water contamination; rather, it serves as a potential chelating agent to evaluate the robustness of the Ru(II) assembly [57]. Carbonate and phosphate, two anions commonly present in natural water, were selected for their basic character and their prevalence in aqueous systems, while other anions are standard competitors in anion binding studies [8].

The MRDPP assembly has four lactam NH protons, which are potentially acidic and can exhibit proton-donating ability. These NH protons can therefore interact with anions either via hydrogen bond- or anion-induced deprotonation. As shown in Figure 4a, MRDPP has a notable selectivity for CN^- relative to other anions. MRDPP exhibits the highest UV-vis response toward cyanide, followed by carbonate and to a lesser extent phosphate. Upon interaction with these basic anions (pK_a values: HCN = 9.2, HPO_4^{2-} = 12.3, HCO_3^{2-} = 10.0; Table S1), a clear red-shift in the maximum of the absorption band from 540 nm to 595 nm was exclusively observed with CN^-, suggesting the formation of a deprotonated MRDPP and production of HCN [58]. On the other hand, the addition of PO_4^{3-} resulted in a decrease in the intensity of the absorbance at 540 nm without a significant shift, suggesting

minimal interactions. For CO_3^{2-}, the response was also moderate, with a slight red-shift from 540 nm to 547 nm accompanied by reduced intensity, as well as the emergence of a new band around ≈595 nm, suggesting deprotonation of MRDPP. These different responses are probably due to the difference in the free hydration energy of the anions (Table S1). The CN^- has the lowest hydration energy (−295 kJ/mol) and thus interacts more easily in aqueous media with the NH protons of MRDPP. In contrast, PO_4^{3-} and CO_3^{2-} possess higher hydration energies, −3888 and −2127 kJ/mol, respectively, which stabilize their hydrated forms and reduce their availability for interaction with MRDPP in water.

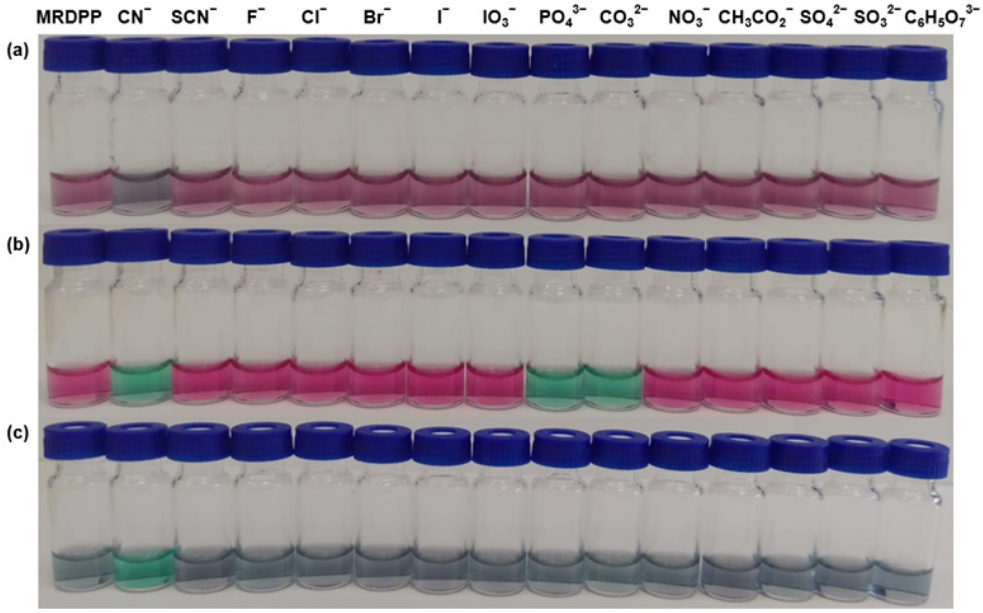

Figure 3. Visual response of MRDPP (25 μM, 1 eq.) upon addition of anions (1 mM, 40 eq.) in different solvents: (**a**) distilled water (+0.025% *v*/*v* of methanol); (**b**) acetonitrile; (**c**) ethanol.

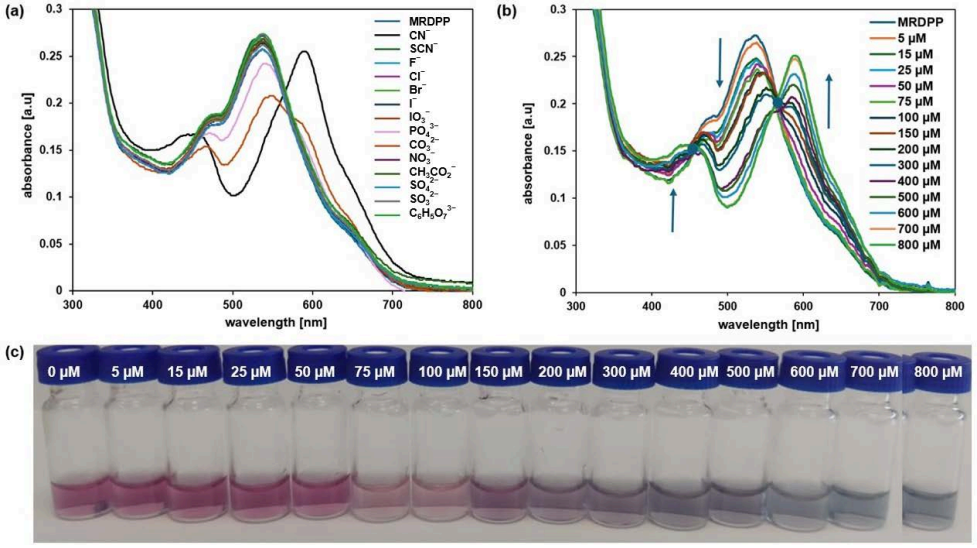

Figure 4. (**a**) UV-vis absorption spectra of MRDPP (25 μM, 1 eq.) in distilled water (+0.025% *v*/*v* of methanol) upon addition of anions (1 mM, 40 eq.). (**b**) UV–vis absorption spectra of MRDPP (25 μM) in water at different concentrations of cyanide (0–800 μM). (**c**) Visual color changes of MRDPP (25 μM) in water upon gradual addition of cyanide (0–800 μM).

A UV-vis spectrophotometric titration was carried out in water (Figure 4b) with a 25 μM aqueous solution of MRDPP with increasing concentrations of cyanide (0–800 μM).

From the spectroscopic data, it is clear that upon the progressive addition of CN^-, the maximum absorbance intensity at 540 nm gradually reduced and endured a bathochromic shift (~20 nm), while simultaneously a new band at 595 nm appeared with clear isosbestic points at 564 nm, revealing the formation of a second species in solution. Figure 4c shows the colorimetric response of MRDPP during the CN^- titration; a pronounced color change of the solution during the titration demonstrates the colorimetric potential of the sensor for not only recognizing the presence of cyanide but also its concentration.

A possible explanation of the ratiometric changes in absorption is the intermolecular process involving the lactam NH protons of MRDPP and cyanide ions (Scheme 2). A transformation occurs from the initial complex, MRDPP, with four lactam NH protons, to the deprotonated form of the complex and release of HCN. Deprotonation can be considered as an electron transfer to the nitrogen atom, which increases the electron density and induces the delocalization of the electron throughout the DPP unit and thus leads to a more pronounced bathochromic shift [58,59]. The delocalization of electrons is facilitated by the internal electrostatic forces between the negatively charged nitrogen of DPP and the Ru(II) centers via the pyridyl groups (Figure S6). The proton transfer exhibits similar behavior to an intramolecular charge transfer, where in the absence of CN^- in solution, the neutral amide is not considered as a donor. However, in the presence of CN^-, the NH is deprotonated and the nitrogen atom acts as a donor, while the other components of MRDPP serve as acceptors. This delocalization of electrons explains the red-shift in the absorbance upon addition of CN^-. To validate this assumption, ^{1}H NMR of MRDPP was conducted in DMSO-d_6 with and without cyanide (Figure 5). Upon addition of four equivalents of CN^-, the NH signal (~11.7 ppm) disappeared completely. Moreover, the release of HCN from the DMSO solution can be demonstrated by placing a pH-indicator strip on top of the bottle, which reacts with acidic HCN vapors (Figure S7), thus further confirming the proposed sensing mechanism.

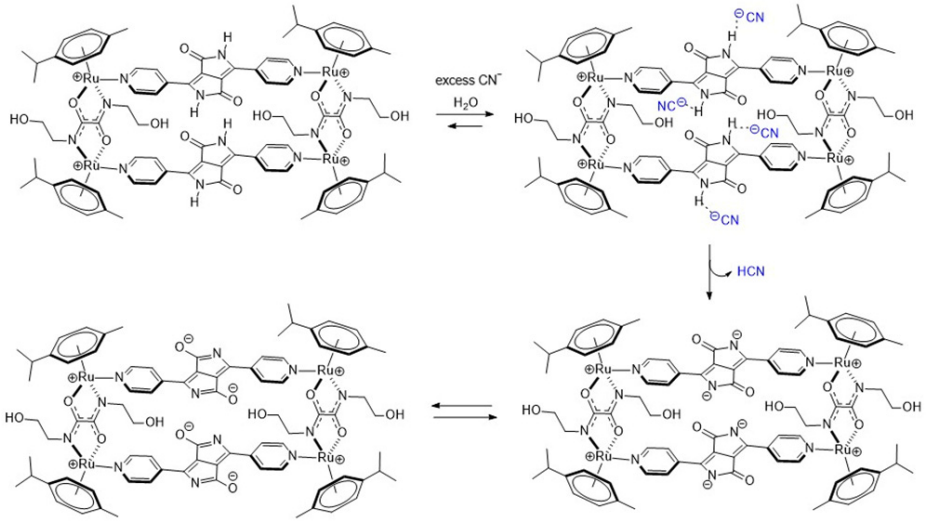

Scheme 2. Proposed proton transfer mechanism between MRDPP and cyanide.

The stoichiometry of the MRDPP–cyanide interactive system in water was established via a Job plot analysis. A crossover point at 0.8 suggests a 1:4 [MRDPP]·$(CN^-)_4$ binding system (Figure S8). Beyond this threshold, the absorbance slightly decreases. MRDPP is a multi-site system with different functional groups, not only the acidic lactam hydrogens, but also the positively charged dinuclear Ru(II) bis(2-hydroxyethyl)ethanediamide clips, adding a residual level of weak interactions with CN^- that remains detectable even after formation of the stronger 1:4 system. Absorbance titration reveals a binding-equilibrium

constant of 8.74 ± 0.9 × 10^3 M^{-1} between MRDPP and CN^- (Figure S8). This binding constant suggests a moderate affinity of MRDPP towards cyanide in water. The detection limit (LOD) was found to be 4.0 μM (Figure S9); this estimated value does not fall below the WHO-permitted limit of 1.9 μM, but it is close. In general, low LOD values are obtained in organic solvents using highly sensitive techniques such as fluorescence [60], while most sensing systems based on absorption methods have LOD values in the upper micromolar range [30].

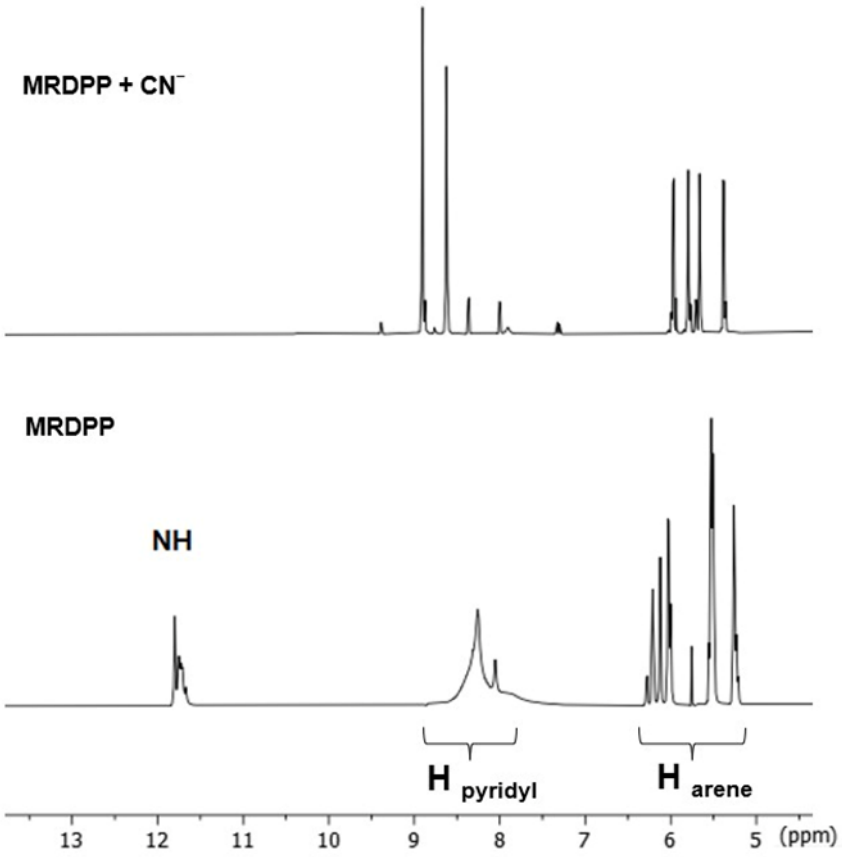

Figure 5. ^{1}H NMR spectra (aromatic region, DMSO-d_6) of MRDPP upon addition of 4 equivalents of cyanide.

A competitive experiment was carried out by mixing MRDPP with multiple anions (10 equivalents each) but excluding cyanide (Figure S10). This experiment showed that the aqueous solution remains pink in the presence of SCN^-, F^-, Cl^-, Br^-, I^-, IO_3^-, PO_4^{3-}, CO_3^{2-}, NO_3^-, $CH_3CO_2^-$, SO_4^{2-}, SO_3^{2-} and $C_6H_5O_7^{3-}$. On the other hand, when 10 equivalents of CN^- were added to this solution, a distinct color change from pink to greyish-blue was observed, confirming the strong affinity and selectivity of MRDPP towards CN^-. This result highlights that cyanide detection remains effective in the presence of other common anions.

Determination of the pKa: Considering the proposed mechanism involving deprotonation of the DPP units in the presence of CN^- (Scheme 2), the pKa values of MRDPP were assessed experimentally from potentiometric titrations. The first titration of MRDPP with NaOH (MRDPP at a 2 × 10^{-3} M concentration in a pH = 6.2 Britton–Robinson buffer solution) [61] provided three pKa values, pKa_1 = 6.8, pKa_2 = 8.5 and pKa_3 = 9.4 (Figure S11a). However, the last equivalence point was not observed, forcing us to run a second titration at the same concentration with a different buffer solution of MRDPP (pH = 10 Britton–Robinson buffer solution). The last pKa value was estimated at 10.3 (Figure S11b). The pH

of the buffer solution necessary to dissolve MRDPP wasselected from the pKa values of the bipyridyl–DPP unit (pKa_1 = 8.2, pKa_2 = 9.5), which were determined empirically via the Chemaxon software (version 1.6.2) [62].

A spectrophotometric titration (MRDPP at a 10^{-4} M concentration) was also performed over a 3-to-13 pH range (Britton–Robinson buffer solutions). Then, the spectra obtained were plotted as a function of the pH (Figure S12), providing two absorption maxima at 520 nm for pH = 3.0 and 594 nm at pH = 13.0. From these two wavelengths, the corresponding pKa values (6.9 and 11.3) were determined using a modified Henderson–Hasselbalch equation. The first pKa value at 6.9 is believed to be associated with the loss of two protons, one proton per DPP unit. Then, the remaining protons of the two DPP units are removed, giving rise to the second pKa value at 11.3. Overall, these different titrations are both in agreement with the proposed mechanism.

Theoretical calculations: To better understand MRDPP behavior in solution and to validate our proposed mechanisms, DFT calculations were performed at the PBE0 level of theory on the intact MRDPP assembly [63], as well as on the deprotonated intermediates. In all calculations, benzene was used in place of *p*-cymene to reduce the electron count and thereby to minimize the computational costs.

As previously discussed, different conformations (syn- and anti-) of MRDPP can be obtained, according to the orientation of the DPP units. DFT calculations suggest that the syn-conformation is energetically favored by 1.24 kcal·mol^{-1} (Table S2). The calculated UV-vis spectrum of syn-MRDPP perfectly reproduces the experimental trace (Figure 6), whereas anti-MRDPP shows some variations (Figure S13). Despite these negligible energy differences, we cannot rule out a possible contribution from anti-MRDPP. Nevertheless, all calculations were performed on the syn-MRDPP assembly and its deprotonated derivatives. In the UV-vis of syn-MRDPP, the weak absorption at about 950 nm is described by two transitions involving HOMO, LUMO, HOMO-1 and LUMO+1, while the absorption at 550 nm considers also higher- and lower-energy orbitals. For the shapes and energies of the orbitals (Figure S14) and a full description of the electronic transitions (Table S3), see the Supplementary Materials.

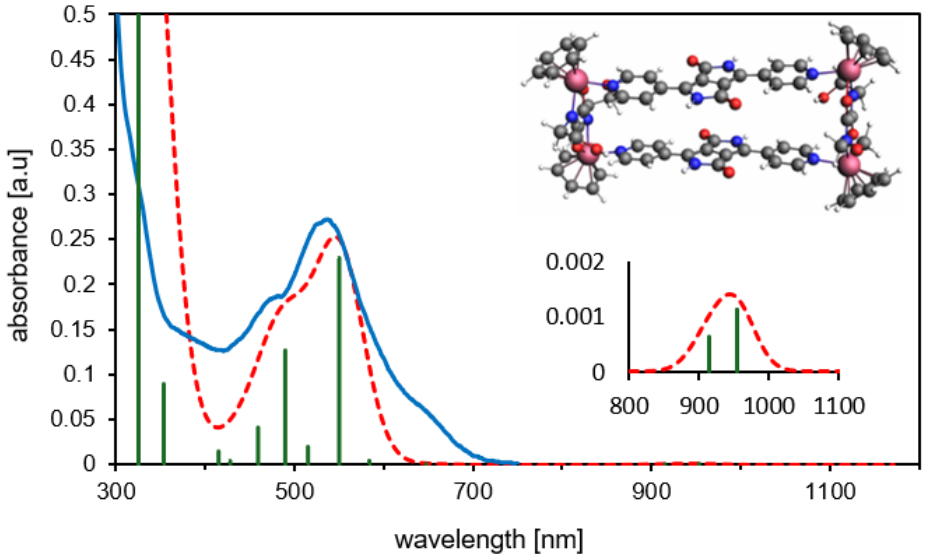

Figure 6. Experimental (blue) vs. theoretical (TD-DFT/PBE0, dashed red) UV-vis spectra for syn-MRDPP. The green vertical bars represent the oscillator strengths for the main absorptions. Inset: expansion of the less intense band appearing at about 950 nm.

The optimized structures (*xyz* coordinates) and the associated energies (Table S2) can be found in the Supplementary Materials. In the syn-MRDPP assembly, the mean

Ru-C(benzene) bond distances (2.20–2.23 Å) fall in the range of reported X-ray structures (2.11–2.24 Å) [64,65]. Consequently, the Ru-centroid distances also align well with data in the literature (1.70 Å for syn-MRDPP, 1.64–1.69 Å experimental) [64,65]. This further validates our model and confirms the proposed metalla-rectangle assembly of MRDPP. Atomic charges have been computed according to Voronoi deformation density (VDD) [66] and Hirshfeld methods [67] (Figure S15) for the benzene analogue of MRDPP (starting with the 4+ cation) and its deprotonated derivatives. These analyses suggest that the first two deprotonation reactions occur "alternatively" on two DPP groups of different bridging units.

Recyclability using iron(III) chloride: Good reproducibility and reversibility of sensors are essential for industrial applications, as well as for sustainable detection technologies [68,69]. Cyanide is well known in coordination chemistry, being a strong π-acceptor ligand that is able to bind to many transition metals, including but not limited to Cu^{2+}, Ni^{2+} and Fe^{3+} [70]. As Fe^{3+} is abundant and cheap, and because it forms a very stable and non-toxic complex with cyanide $[Fe(CN)_6]^{3-}$ ($K_f = 7.94 \times 10^{43}$) [71], we used an $FeCl_3$ solution to test the regeneration capacity of MRDPP (Scheme S1).

Multiple cycles were carried out in distilled water with 0.025% (*v*/*v*) methanol, alternating cyanide and $FeCl_3$ solutions. A solution of CN^- (400 µM) was added to a solution of MRDPP (25 µM); when saturation was reached (about a 30.8% decrease in the absorbance at 540 nm), a 68 µM solution of Fe^{3+} was added, resulting in an increase in the absorbance, showing that the complex formed between Fe^{3+} and CN^- was more stable than the $[MRDPP]^{4+}\cdot(CN^-)_4$ adduct. A second addition of CN^- resulted, again, in a loss of 30.7% of the absorbance intensity, which was recovered after the addition of $FeCl_3$. Twelve cycles were performed, and the ratio between the MRDPP absorbance before and after the addition of the CN^- solution was always around 30% (Figure 7). The $[Fe(CN)_6]^{3-}$ complex is yellow, showing an absorbance around 440 nm (Figure S16). After cycle 6, the concentration of $[Fe(CN)_6]^{3-}$ increases, which causes a blue-shift in the absorbance of regenerated MRDPP and gives a brighter color (Figure 7c). Interestingly, this change in the absorbance did not affect the visual detection of cyanide. After the last cycle, MRDPP was isolated by precipitation and ESI-MS spectrometry revealed a peak at *m*/*z* 467.59 corresponding to the intact sensor $[MRDPP]^{4+}$ (Figure S17).

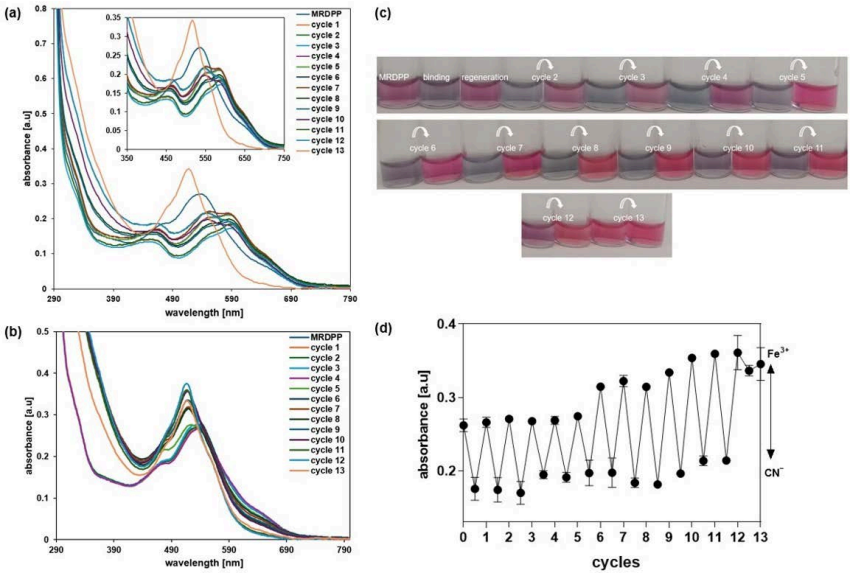

Figure 7. (**a**) UV-vis absorption spectra of MRDPP in the presence of CN^- over multiple cycles with Fe^{3+}. (**b**) UV-vis absorption spectra of regenerated MRDPP. (**c**) Visible color changes of MRDPP during the alternance addition of CN^- and Fe^{3+}. (**d**) Absorbance intensity at 540 nm after each cycle.

Besides the in situ regeneration of MRDPP, an ex situ experiment (isolated conditions) was also performed based on the isolation of MRDPP at the end of each cycle. The solvent was removed under vacuum, then pure water was added to the residue, triggering the precipitation of MRDPP as a red solid, and the water-soluble $[Fe(CN)_6]^{3-}$ complexes were removed by filtration. As shown in Figure 8a,b, no loss in the efficiency of MRDPP sensing was observed, as the absorbance remained the same over four cycles. In addition, the same behavior of cyanide sensing was observed, as well as the visual color changes (Figure 8c), confirming that MRDPP is a reversible, robust and reusable sensor in distilled water with 0.025% (v/v) methanol.

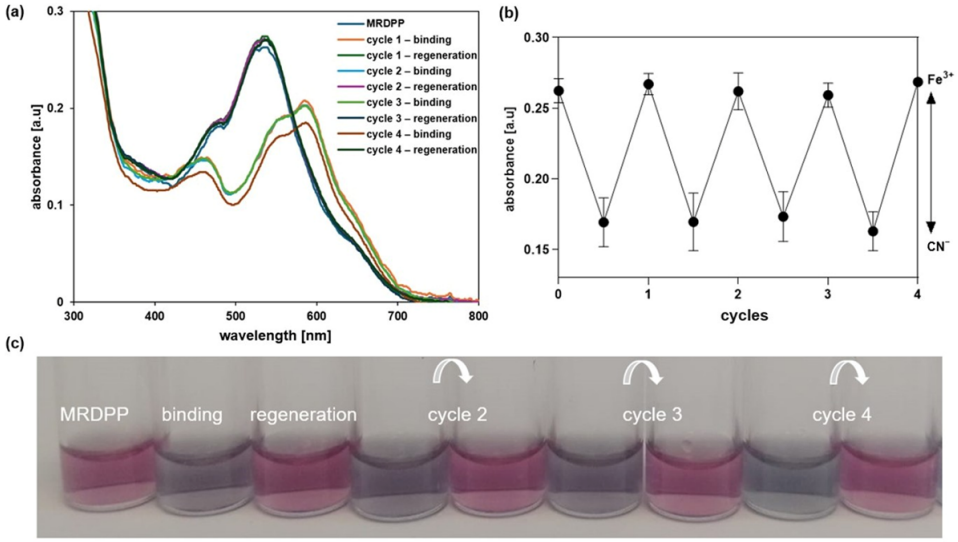

Figure 8. (**a**) UV-vis absorption spectra of MRDPP showing the reversible response of MRDPP upon CN^- binding and Fe^{3+} assisted regeneration. (**b**) Absorbance of MRDPP at 540 nm in the presence of CN^- before and after addition of Fe^{3+}. (**c**) Color changes before and after (4 cycles).

Nucleophilic addition-driven cyanide sensing at pH 8: We have determined that MRDPP acts as a colorimetric sensor for CN^-, CO_3^{2-} and PO_4^{3-}, with some degree of selectivity towards CN^- in water, through a proton transfer mechanism. Therefore, the pH is an important factor, and controlling the proton transfer propensity of DPP is a parameter that can be adjusted. Indeed, the selectivity is greatly enhanced in HEPES buffer (pH 8) solutions, in which MRDPP behaves as a selective sensor for CN^-. At a slightly basic pH, the UV–vis absorption spectra of MRDPP are only affected by the presence of CN^- (Figure 9a), in sharp contrast to the results obtained in distilled water + 0.025% v/v of methanol (Figure 4a), where basic anions like CO_3^{2-} and PO_4^{3-} also interact with MRDPP. At pH 8, only the presence of CN^- induces a decrease in the absorbance intensity, with no red-shift, suggesting that deprotonation does not occur under basic conditions and that a different recognition mechanism is involved. At a high cyanide concentration, the decrease in the absorbance intensities at 474 and 540 nm is accompanied with a splitting of the absorbance band at 540 nm into two distinct maxima (Figure 9b), shifting the MRDPP solutions from pink to gray (Figure 9c).

In distilled water, cyanide is partially hydrolyzed and an equilibrium between CN^- and HCN is at play, which overall reduces the nucleophilicity of cyanide. On the other hand, under slightly basic conditions (HEPES buffer (pH 8)), this equilibrium mostly shifts toward the CN^- form, thus increasing CN^- nucleophilicity towards electrophiles and accordingly switching the target from the NH protons of DPP to the adjacent carbonyl groups. Such reactions of electrophilic carbonyl compounds with CN^- are known in the literature [72], particularly with electron-deficient amides [73]. Based on this fact and facilitated by the

presence of an electron-deficient DPP backbone and a positively charged Ru-based assembly, the electrophilic carbonyl carbon atoms in DPP undergo 1,2-nucleophilic additions with cyanides, resulting in the formation of cyanide adducts (Scheme 3). Under basic conditions, intermediates I and III are unable to protonate and form stable species, so a rearrangement occurs after the loss of OH^-, generating new assemblies (Forms II and IV, Scheme 3). The driving force of this rearrangement is the generation of more energetically stable systems by extensive conjugation through the bipyridyl–DPP spacers. This pathway of cyanide sensing by MRDPP was confirmed by ESI-MS spectrometry, where at four equivalents of CN^-, a peak at *m/z* 472.58 was observed, indicating the addition of two CN^- groups to the system [MRDPP + 2 **CN** – 2 **OH**]$^{4+}$ (Figure S18b). Upon increasing the amount of CN^- to 25 equivalents, a new peak at *m/z* 477.60 was detected, corresponding to the formation of the proposed form, IV [MRDPP + 4 **CN** – 4 **OH**]$^{4+}$, with four cyanide groups replacing the four oxygen atoms of DPP (Figure S18c). Therefore, by modifying the pH of the aqueous medium, we were able to modulate the cyanide sensing mechanism of MRDPP. Under such conditions, the detection limit of MRDPP towards CN^- was estimated to be 55.3 μM (Figure S19). The infrared spectra of MRDPP before and after the addition of cyanides were measured (Figure S20), showing the appearance of typical nitrile bands at 2240 and 2370 cm^{-1}.

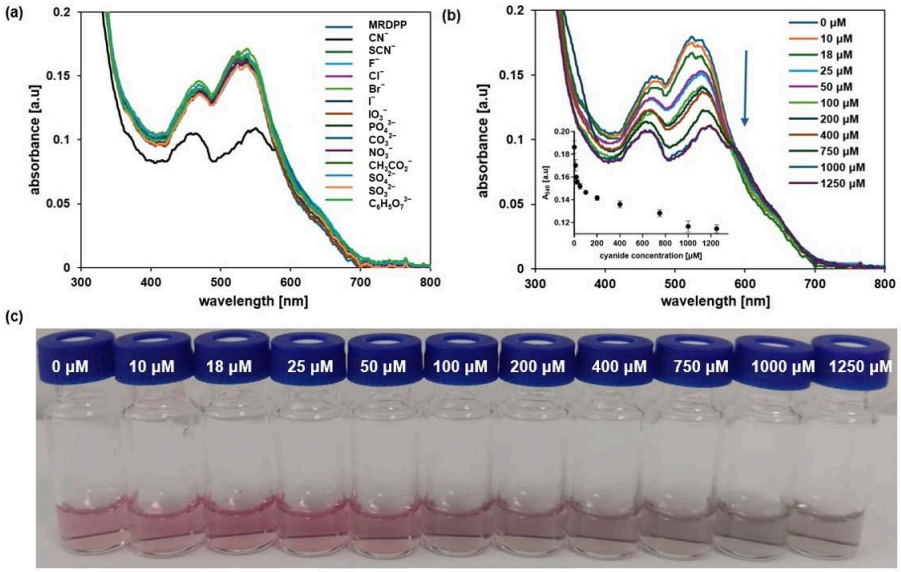

Figure 9. (**a**) Variation in absorption of MRDPP (25 μM, 1 eq.) in HEPES buffer (pH 8) upon addition of anions (1 mM, 40 eq.). (**b**) Variation in absorption of MRDPP (25 μM) in HEPES buffer (pH 8) upon successive additions of cyanide (0–1250 μM). Inset: The change in absorbance at 540 nm with different concentrations of CN^-. (**c**) Visual color changes of MRDPP (25 μM) in HEPES buffer (pH 8) upon titration with CN^- (0–1250 μM).

Test strip experiments: For practical application purposes, the responsiveness of the MRDPP sensor as a chromogenic test strip in HEPES buffer (pH 8) was determined. MRDPP-coated Macherey–Nagel filter paper was prepared by immersing the filter paper in a pH 8 buffered solution of MRDPP (25 μM) and drying it in air for 10 min. The color of the paper changed from pink to gray when the coated strip was dipped in a CN^- solution (1 mM), whereas there was no color change with other anions, as shown in Figure 10a. Test strip-based titration of MRDPP with cyanide shows an intensifying gray tone with increasing concentrations of cyanide (50–200 μM) (Figure 10b). These simple tests suggest that test strips using the MRDPP sensor can potentially produce, after some optimization experiments, a low-cost colorimetric kit for cyanide detection in aqueous media.

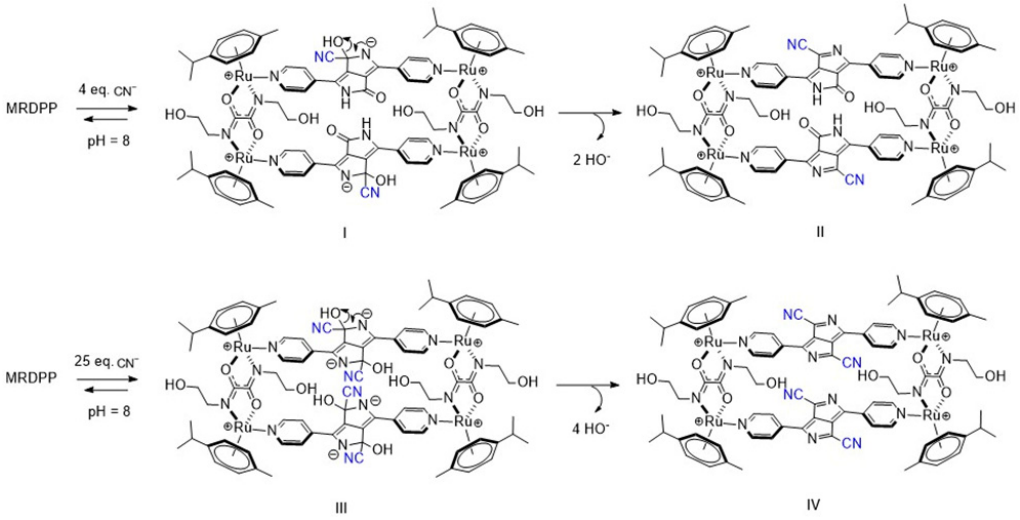

Scheme 3. Intermediates observed upon addition of cyanides to MRDPP in HEPES buffer (pH 8).

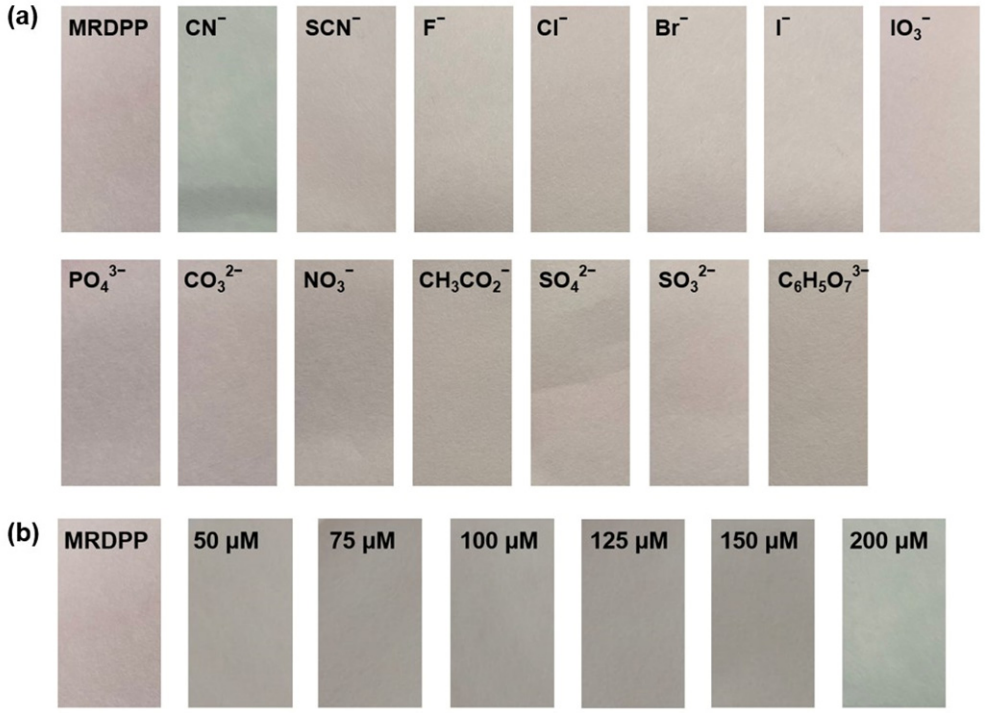

Figure 10. (**a**) Visual response of MRDPP (25 μM)-based test strips towards various anions (1 mM) in HEPES buffer (pH 8). (**b**) Test strips of MRDPP with increasing cyanide concentrations.

3. Materials and Methods

3.1. Materials

All chemicals and solvents were purchased from Sigma-Aldrich (Darmstadt, Germany) and used as received. [Ru_2(*p*-cymene)$_2${*N*,*N*′-bis(2-hydroxyethyl)oxamidate}Cl_2] [74] and 3,6-di(pyridin-4-yl)-2,5-dihydro pyrrolo [3,4-c]pyrrole-1,4-dione [75] were prepared according to reported methods. Stock solutions of salts (0.1 M), including NaCN, NaSCN, NaF, NaCl, NaBr, NaI, $NaIO_3$, Na_3PO_4, Na_2CO_3, $NaNO_3$, $NaC_2H_3O_2$, Na_2SO_4, Na_2SO_3, $Na_3C_6H_5O_7$ and $FeCl_3$, were prepared from distilled water. Stock solution of MRDPP (0.1 M) was prepared in MeOH. Working solutions of MRDPP and anions were obtained by diluting the stock solutions with distilled water and 20 mM HEPES buffer (pH 8) (0.025% v/v of methanol). Robinson−Britton buffers were prepared from boric acid, acetic acid

and phosphoric acid solutions. The pH of solutions was adjusted using solid NaOH and regulated with a FiveEasy METTLER TOLEDO® pH meter (Mettler Toledo, Griefensee, Switzerland). Due to the high toxicity of HCN, which is released upon detection in water, all manipulations should be performed under a fume hood with standard safety protocols.

3.2. Instrumentation

The ^{1}H, ^{13}C{^{1}H} and DOSY NMR spectra were recorded on a Bruker Avance II 600 MHz (Bruker, Manheim, Germany) at 23 °C in MeOD and DMSO-d_6 and referenced relative to residual solvents, 3.3 and 2.5 ppm, respectively. Multiplicities are reported in Hz as follows: s = singlet, d = doublet, t = triplet, q = quartet and m = multiplet. Electrospray ionization mass spectra were obtained in positive ion mode on an LTQ Orbitrap Elite instrument at the ISIC Mass Spectrometry Service (SSMI) in Lausanne (Switzerland). UV-vis spectra were recorded with a thermostatted VICTOR® Nivo™ multimode plate reader (Avantor, Dietikon, Switzerland). The infrared spectra were recorded in solid form at the Haute École Arc campus in Neuchâtel using a Thermo Scientific (Reinach, Switzerland)™ Nicolet™ iD5 ATR (Attenuated Total Reflectance) coupled to a FTIR spectrometer.

3.3. Synthesis and Characterization of MRDPP

A mixture of [Ru_2(*p*-cymene)$_2${*N*,*N*′-bis(2-hydroxyethyl)oxamidate}Cl_2] (100 mg, 139.6 µmol, 2 equiv.) and $AgCF_3SO_3$ (71.8 mg, 279.5 µmol, 4 equiv.) in anhydrous methanol (15 mL) was stirred at rt for 2 h. Then, the solution was filtered to remove AgCl. The 3,6-di(pyridin-4-yl)-2,5-dihydropyrrole [3,4-c]pyrrole-1,4-dione (40.5 mg, 139.7 µmol, 2 equiv.) was added, and the solution was stirred at rt for 48 h. The solvent was removed under vacuum, and the residue was redissolved in methanol (2 mL). Diethyl ether was slowly added to initiate precipitation of the product as a dark-pink solid, with a yield of 98% (168 mg, 69.8 µmol). Chemical formula: $C_{88}H_{96}F_{12}N_{12}O_{24}Ru_4S_4$. MW = 2464.8 g·mol^{-1}.

^{1}H NMR (600 MHz, MeOD) δ 8.7–7.8 (m, 16H, $CH_{pyridyl}$, 6.2–5.8 (m, 8H, $CH_{p\text{-cym}}$), 5.8–5.4 (m, 8H, $CH_{p\text{-cym}}$), 4.3–3.8 (m, 16H, CH_2), 2.8 (dtd, J = 14.9, 10.6, 3.9 Hz, 4H, $CH(CH_3)_2$), 1.8–1.7 (m, 12H, $CH(CH_3)_2$), 1.6 (m, 12H, CH_3), 1.3 (d, J = 6.9 Hz, 12H, $CH(CH_3)_2$). ^{13}C NMR (151 MHz, MeOD) δ 173.0 (CH_2NC=O), 162.8 (HNC=O_{DPP}), 155.6 (N=$CH_{pyridyl}$), 137.1 (=C-CNH_{DPP}), 122.8 (=C-NH_{DPP}), 120.8 (=$CH_{pyridyl}$), 105.2 (=C-C=O_{DPP}), 98.9 ($CH_{p\text{-cym}}$), 87.5 ($CH_{p\text{-cym}}$), 85.6 ($CH_{p\text{-cym}}$), 84.8 ($CH_{p\text{-cym}}$), 81.5 ($CH_{p\text{-cym}}$), 61.9 (CH_2-OH), 56.1 (N-CH_2), 39.6 ($CH(CH_3)_2$), 32.4 ($CH(CH_3)_2$), 23.1 ($CH(CH_3)_2$), 22.1 ($CH(CH_3)_2$), 17.8 (CH_3). ESI−MS: *m*/*z* = 467.6 [MRDPP–4$CF_3SO_3^-$]$^{4+}$, 673.4 [MRDPP–3$CF_3SO_3^-$]$^{3+}$.

3.4. pK$_a$ Determination

To determine the pKa values of MRDPP, spectrophotometric and pH-metric titrations were carried out: Spectrophotometric titration: The experiment was carried out at rt using 96-well NUNC® transparent plates (Thermo Fisher Scientific, Reinach, Switzerland) and 0.1 M stock solution of MRDPP in methanol. Robinson–Britton buffer solutions (0.04 M each of acetic acid, phosphoric acid and boric acid) were prepared by adjusting the pH using 0.2 M of aqueous NaOH solution to obtain a pH range of 3 to 13. Then, 1.0×10^{-4} M sample solutions of MRDPP were prepared in different buffered solutions, and the absorption spectra of the solutions were recorded. The absorbance values obtained were plotted as a function of the pH. The pKa values were determined via the following equation [76,77].

$$\mathrm{pH} = \mathrm{pKa} - \log\left(\frac{A - A_0}{A_f - A_0}\right)$$

pH-metric titration: The experiment was carried out at rt using a calibrated pH meter and 0.1 M stock solution of MRDPP in methanol. Then, a 2.0×10^{-3} M sample solution of MRDPP was prepared by diluting MRDPP in 20 mL of Robinson−Britton buffer (0.007 M, pH 6.6 or pH 10). A titrant solution of NaOH (0.05 M) was added dropwise under constant magnetic stirring. The pH value and the volume of NaOH were recorded after equilibration for 5 min. The obtained data were plotted, and the first derivative ($\Delta pH/\Delta V$) was calculated to determine the inflection points, corresponding to the pKa values of MRDPP [78,79].

3.5. DFT Calculations

All calculations were carried out at the density functional (DFT) level of theory with the ADF2021.102 program package [80–82]. The PBE0 functional was employed for all calculations. TD-DFT implemented in the ADF package was used to determine the excitation energies: the 30 lowest singlet–singlet excitations were calculated using optimized geometries. For geometry optimizations, C, N and O atoms were described through TZ2P basis sets [triple-ξ, Slater-type orbitals (STOs) plus two polarization functions]; Ru was described through QZ4P basis sets [quadruple-ξ, Slater-type orbitals (STOs) plus four polarization functions]; and H atoms were described through TZP [triple-ξ, Slater-type orbitals (STOs) plus one polarization function]. The corresponding augmented basis set was employed in TD-DFT calculations [83]. Restricted formalism, no-frozen-core approximation (all-electron) and no-symmetry constraints were used in all calculations. Solvent effects (water) were simulated by employing the conductor-like continuum solvent model (COSMO) [84–86] as implemented in the ADF suite.

3.6. General Spectroscopic Procedure

Spectroscopic measurements were carried out at 25 °C using transparent NUNC® 96-well plates. The absorption spectra were recorded at a final MRDPP concentration of 25 μM after an equilibration period of 10 min. Baseline corrections were applied using the respective solvents as a reference. Screening experiments were performed in distilled water and 20 mM HEPES buffer (pH 8). For the titration experiments, an initial MRDPP stock solution of 100 μM was prepared in methanol, while a cyanide aqueous solution was used at a concentration of 2500 μM. The titration curves were recorded and analyzed using Excel and Prism 5.0® version software [87,88].

3.7. Detection Limit Determination

The detection limits for cyanide were determined using absorbance titration profiles of MRDPP with cyanide. The limit of detection (LOD) was calculated using the standard equation: LOD = 3σ/S, where σ represents the standard deviation obtained from 10 blank measurements and S is the slope derived from the calibration curve [89].

3.8. Calculation of Binding Constant (K)

The binding constants of MRDPP for cyanide were calculated from the absorption titration profiles using the isotherm binding model with the following modified equation:

$$A_{\text{obs}} = \frac{A_0 + A_\infty K[\text{CN}^-]_T}{1 + K[\text{CN}^-]_T}$$

where A_{obs} is the observed absorbance at a given concentration of cyanide, A_0 is the absorbance of the free MRDPP, A_∞ is the absorbance at saturation, K is the binding constant and $[CN^-]_T$ is the total concentration of cyanide [90]. Titrations for the determination of the binding constants were performed in triplicate, and the average value was reported.

3.9. Paper Strip Experiments

Low-cost strips of test paper were prepared by dipping precisely cut strips of Macherey–Nagel filter paper in a 25 μM solution of MRDPP in a HEPES buffer (pH 8). The treated strips were then removed, dried in the air for 10 min and immersed in solutions of various selected anions (1 mM). In contact with cyanide solutions, immediate visual color changes were observed, while no significant color changes were noted even after 15 min of exposure to other anions.

3.10. Regeneration of MRDPP

The regeneration experiments were conducted in a 100 μL well with a 25 μM MRDPP solution and 400 μM CN^- (16 equivalents), corresponding to a signal close to saturation. To this mixture, 68 μM of Fe^{3+} (2.7 equivalents) was added. The mixture was left to stand for 10 min before recording the absorbance. The regeneration was carried out both in situ and ex situ. In the in situ experiment, the sensor was regenerated by precipitation at the end of all cycles. In the ex situ experiment, the sensor was precipitated at the end of each cycle.

Since $[Fe(CN)_6]^{3-}$ was soluble under the detection conditions (water + 0.025% v/v methanol), a precipitation experiment was carried out by eliminating the solvent under vacuum conditions, then dissolving the residue in 100 μL of water. A small amount of red precipitation was observed, and the water was removed using a micropipette. This process was repeated three times to ensure that no cyanide remained.

For the ex situ (isolated conditions) experiments, the precipitate was redissolved in order to continue the following cycles using 25 μL of a solvent mixture (1 μL of methanol and 999 μL of water).

3.11. ATR-FTIR Measurement Procedure

Each sample was placed directly onto the ATR crystal as a powder (solid form). IR spectra were collected in the range of 4000–500 cm^{-1}. A background spectrum was recorded before each measurement and subtracted from the sample spectra. All spectra were measured at room temperature.

4. Conclusions

In summary, we have developed the first arene ruthenium metalla-assembly (MRDPP) as a selective colorimetric sensor for cyanide in water. MRDPP can be synthesized in a single step (98% yield) and in good quantities. The sensor exhibits significant selectivity towards cyanide, and the sensitivity was estimated to be in the micromolar range (4 μM), in accordance with the World Health Organization's recommended permissible level [6]. MRDPP shows medium-dependent dual mechanisms for cyanide detection: in water, the recognition follows a proton transfer of the acidic NH to the basic CN^-, leading to a red-shift in the absorbance, while at pH 8, the sensing proceeds via nucleophilic addition, where CN^- attacks the electrophilic carbonyl of DPP, leading to a decrease in the absorbance intensity and the formation of a new complex. These different mechanisms were confirmed by UV-vis spectroscopic titrations, ^1H NMR and ESI-MS spectrometry. DFT calculations were carried out to better understand the electronic structures of the free assembly and its deprotonated forms to support our experimental observations. One of the most remarkable aspects of MRDPP is its recyclability in water using Fe^{3+} solution. Based on these characteristics, MRDPP can be used for practical applications, such as on-site cyanide detection or environmental monitoring, showing, overall, that arene ruthenium assemblies are excellent scaffolds for producing versatile chemosensors.

Supplementary Materials: The following supporting information can be downloaded at https://www.mdpi.com/article/10.3390/inorganics13110357/s1: Synthesis and characterization: ^{1}H, ^{13}C and DOSY NMR spectra, MS spectra, detection limit plots, binding constant plots, UV−vis spectra, DFT data, xyz coordinates. Figure S1. ^{1}H NMR spectrum of MRDPP in MeOD; Figure S2. $^{13}C\{^{1}H\}$ NMR spectrum of MRDPP in MeOD; Figure S3. DOSY NMR spectrum of MRDPP in MeOD; Figure S4. ESI−MS spectrum of MRDPP (positive ion mode); Figure S5. Syn and anti conformations of MRDPP; Figure S6. Delocalization of electrons through the π-system after deprotonation; Figure S7. pH-indicator strips showing the HCN released from a DMSO solution containing MRDPP (1 mM) and cyanide (4 mM), as control experiment (NaCN in DMSO, a drop of solution after 10 min); Figure S8. Fit of the experimental absorbance data at 540 nm upon addition of increasing concentration of cyanide in distilled water; Figure S9. Determination at 540 nm of the LOD for cyanide with MRDPP (25 μM, distilled water); Figure S10. Competitive anionic binding experiments with MRDPP in distilled water. Photograph of the MRDPP solution (25 μM) in the presence of 10 equiv. of each anions (SCN^-, F^-, Cl^-, Br^-, I^-, $IO_3{}^-$, $PO_4{}^{3-}$, $CO_3{}^{2-}$, $NO_3{}^-$, $CH_3CO_2{}^-$, $SO_4{}^{2-}$, $SO_3{}^{2-}$, $C_6H_5O_7{}^{3-}$) on the right, and after addition to that solution of CN^- 10 equiv. on the left; Figure S11. pH titration curve of MRDPP (2.0×10^{-3} M) titrated with NaOH (0.05 M) at rt and constant stirring in: (a) Robinson buffer pH 6.2; (b) Robinson buffer pH 10; Figure S12. (a) UV- vis spectra of MRDPP (1×10^{-4} M) in Robinson buffer at different pHs (3-13); (b) Fit of the absorbance data of MRDPP using a modified Henderson-Hasselbalch equation at two wavelengths (520 nm and 594 nm); Figure S13. Experimental (blue) vs. theoretical (DFT/PBE0) UV-vis spectra for syn-MRDPP (dashed red) and anti-MRDPP (dashed green). Inset: expansion of the less intense band appearing at about 950 nm; Figure S14. Frontier molecular orbitals and relative energies calculated (DFT/PBE0) for syn-MRDPP; Figure S15. Computed atomic charges according to Voronoi deformation density (VDD) and Hirshfeld methods for syn-MRDPP and its deprotonated derivatives. The red arrow indicates the most charged proton, which is removed; Figure S16. (a) UV-vis spectra of MRDPP (25 μM) in the presence of Fe^{3+} (500 μM) and $[Fe(CN)_6]^{3-}$ (500 μM) in distilled water; (b) Colors of MRDPP solutions in the presence of Fe^{3+} and $[Fe(CN)_6]^{3-}$; Figure S17. ESI-MS spectroscopy of MRDPP after the recycling experiment; Figure S18. ESI-MS spectra of; (a) MRDPP alone; (b) MRDPP after addition of 4 equivalents of CN^- ($[MRDPP(\mathbf{CN})_2]^{4+}$); (c) MRDPP after addition of 25 equivalents of CN^- ($[MRDPP(\mathbf{CN})_4]^{4+}$); Figure S19. Determination at 540 nm of the LOD of cyanide with MRDPP (25 μM, HEPES buffer pH 8); Figure S20. FT-IR spectra of MRDPP before (a) and after (b) addition of cyanides; Scheme S1. Regeneration of MRDPP after sensing CN^-, using a $FeCl_3$ solution; Table S1. Hydratation energy of anions and pKa values of the conjugate acids; Table S2. Energies of MRDPP (syn and anti) and the deprotonated intermediates; Table S3. Most important contributions (≥5%) of single orbital transitions to absorptions for syn-MRDPP. Reference [91] is cited in the supplementary materials.

Author Contributions: A.M. carried out the synthesis and characterization, conducted the experiments and data analysis, and wrote the first draft of the manuscript. T.R. and B.T. supervised the research, validated the results and wrote the manuscript. G.C. and S.B. performed the DFT calculations. A.M., T.R. and B.T. contributed to the final version of the manuscript. The manuscript was written through contributions from all authors. All authors have read and agreed to the published version of the manuscript.

Funding: We thank the University of Neuchatel for financial support.

Institutional Review Board Statement: Not applicable.

Informed Consent Statement: Not applicable.

Data Availability Statement: The data supporting this article have been included as part of the Supplementary Materials.

Acknowledgments: We thank G. Attilio Ardizzoia for his valuable input during the DFT calculations.

Conflicts of Interest: The authors declare no conflicts of interest.

References

1. Kruse, F.; Nguyen, A.D.; Dragelj, J.; Schlesinger, R.; Heberle, J.; Mroginski, M.A.; Weidinger, I.M. Characterisation of the Cyanate Inhibited State of Cytochrome c Oxidase. *Sci. Rep.* **2020**, *10*, 3863. [CrossRef]
2. Shimada, A.; Baba, J.; Nagao, S.; Shinzawa-Itoh, K.; Yamashita, E.; Muramoto, K.; Tsukihara, T.; Yoshikawa, S. Crystallographic Cyanide-Probing for Cytochrome c Oxidase Reveals Structural Bases Suggesting that a Putative Proton Transfer H-Pathway Pumps Protons. *J. Biol. Chem.* **2023**, *299*, 105277. [CrossRef] [PubMed]
3. Jaszczak-Wilke, E.; Polkowska, Ż.; Narkowicz, S.; Namieśnik, J. Cyanides in the Environment—Analysis—Problems and Challenges. *Environ. Sci. Pollut. Res.* **2017**, *24*, 15929–15948. [CrossRef]
4. Oesterle, I.; Pretzler, M.; Rompel, A.; Warth, B. Comprehensive Polyphenolic Profiling of Nine Distinct Plants and Edible Mushrooms by Targeted and Untargeted LC-(HR)MS(/MS). *Microchem. J.* **2024**, *200*, 110358. [CrossRef]
5. *GB 5749-2006*; Sanitary Standards for Drinking Water. National Standard of the People's Republic of China: Beijing, China, 2006.
6. World Health Organization. *Guidelines for Drinking-Water Quality*, 2nd ed.; World Health Organization: Geneva, Switzerland, 1996.
7. Randviir, E.P.; Banks, C.E. The Latest Developments in Quantifying Cyanide and Hydrogen Cyanide. *Trends Anal. Chem.* **2015**, *64*, 75–85. [CrossRef]
8. Wang, F.; Wang, L.; Chen, X.; Yoon, J. Recent Progress in the Development of Fluorometric and Colorimetric Chemosensors for Detection of Cyanide Ions. *Chem. Soc. Rev.* **2014**, *43*, 4312–4324. [CrossRef]
9. Chakraborty, S.; Paul, S.; Roy, P.; Rayalu, S. Detection of Cyanide Ion by Chemosensing and Fluorosensing Technology. *Inorg. Chem. Commun.* **2021**, *128*, 108562. [CrossRef]
10. Badugu, R.; Lakowicz, J.R.; Geddes, C.D. Cyanide-Sensitive Fluorescent Probes. *Dyes Pigm.* **2005**, *64*, 49–55. [CrossRef]
11. Schepper, J.; Orthaber, A.; Pammer, F. Tetrazole-Functionalized Organoboranes Exhibiting Dynamic Intramolecular N→B-Coordination and Cyanide-Selective Anion Binding. *Chem. Eur. J.* **2024**, *30*, e202401466. [CrossRef]
12. Lin, Y.-S.; Zheng, J.-X.; Tsui, Y.-K.; Yen, Y.-P. Colorimetric Detection of Cyanide with Phenyl Thiourea Derivatives. *Spectrochim. Acta, Part A Mol. Biomol. Spectrosc.* **2011**, *79*, 1552–1558. [CrossRef]
13. Kumar, A.; Kim, H.-S. A Pyrenesulfonyl-Imidazolium Derivative as a Selective Cyanide Ion Sensor in Aqueous Media. *New J. Chem.* **2015**, *39*, 2935–2942. [CrossRef]
14. Tomasulo, M.; Raymo, F.M. Colorimetric Detection of Cyanide with a Chromogenic Oxazine. *Org. Lett.* **2005**, *7*, 4633–4636. [CrossRef] [PubMed]
15. Chahal, M.K.; Sankar, M. Porphyrin Chemodosimeters: Synthesis, Electrochemical Redox Properties and Selective 'Naked-Eye' Detection of Cyanide Ions. *RSC Adv.* **2015**, *5*, 99028–99036. [CrossRef]
16. Lee, C.H.; Yoon, H.J.; Shim, J.S.; Jang, W.D. A Boradiazaindacene-Based Turn-On Fluorescent Probe for Cyanide Detection in Aqueous Media. *Chem. Eur. J.* **2012**, *18*, 4513–4516. [CrossRef]
17. Mahato, D.; Fajal, S.; Samanta, P.; Mandal, W.; Ghosh, S.K. Selective and Sensitive Fluorescence Turn-On Detection of Cyanide Ions in Water by Post Metallization of a MOF. *ChemPlusChem* **2022**, *87*, e202100426. [CrossRef] [PubMed]
18. Chow, C.-F.; Ho, P.-Y.; Wong, W.-L.; Gong, C.-B. A Multifunctional Bimetallic Molecular Device for Ultrasensitive Detection, Naked-Eye Recognition, and Elimination of Cyanide Ions. *Chem. Eur. J.* **2015**, *21*, 12984–12990. [CrossRef]
19. Fernandes, G.E.; Chang, Y.-W.; Sharma, A.; Tutt, S. One-Step Assembly of Fluorescence-Based Cyanide Sensors from Inexpensive, Off-The-Shelf Materials. *Sensors* **2020**, *20*, 4488. [CrossRef]
20. Rajamanikandan, R.; Sasikumar, K.; Kosame, S.; Ju, H. Optical Sensing of Toxic Cyanide Anions Using Noble Metal Nanomaterials. *Nanomaterials* **2023**, *13*, 290. [CrossRef]
21. Goswami, S.; Manna, A.; Paul, S.; Das, A.K.; Aich, K.; Nandi, P.K. Resonance-Assisted Hydrogen Bonding Induced Nucleophilic Addition to Hamper ESIPT: Ratiometric Detection of Cyanide in Aqueous Media. *Chem. Commun.* **2013**, *49*, 2912–2914. [CrossRef]
22. Padghan, S.D.; Wang, L.-C.; Lin, W.-C.; Hu, J.-W.; Liu, W.-C.; Chen, K.-Y. Rational Design of an ICT-Based Chemodosimeter with Aggregation-Induced Emission for Colorimetric and Ratiometric Fluorescent Detection of Cyanide in a Wide pH Range. *ACS Omega* **2021**, *6*, 5287–5296. [CrossRef]
23. Hua, Y.-X.; Shao, Y.; Wang, Y.-W.; Peng, Y. A Series of Fluorescent and Colorimetric Chemodosimeters for Selective Recognition of Cyanide Based on the FRET Mechanism. *J. Org. Chem.* **2017**, *82*, 6259–6267. [CrossRef]
24. Mandal, M.; Banik, D.; Karak, A.; Manna, S.K.; Mahapatra, A.K. Spiropyran–Merocyanine Based Photochromic Fluorescent Probes: Design, Synthesis, and Applications. *ACS Omega* **2022**, *7*, 36988–37007. [CrossRef]
25. Jung, H.S.; Han, J.H.; Kim, Z.H.; Kang, C.; Kim, J.S. Coumarin-Cu(II) Ensemble-Based Cyanide Sensing Chemodosimeter. *Org. Lett.* **2011**, *13*, 5056–5059. [CrossRef]
26. Liang, C.; Jiang, S. Fluorescence Light-Up Detection of Cyanide in Water Based on Cyclization Reaction Followed by ESIPT and AIEE. *Analyst* **2017**, *142*, 4825–4833. [CrossRef]
27. Nazarian, R.; Darabi, H.R.; Aghapoor, K.; Firouzi, R.; Sayahi, H. A Highly Sensitive "ON–OFF" Optical Sensor for the Selective Detection of Cyanide Ions in 100% Aqueous Solutions Based on Hydrogen Bonding and Water Assisted Aggregation Induced Emission. *Chem. Commun.* **2020**, *56*, 8992–8995. [CrossRef]

28. Wei, T.-B.; Ding, J.-D.; Chen, J.-F.; Han, B.-B.; Jiang, X.-M.; Yao, H.; Zhang, Y.-M.; Lin, Q. A Cyanide-Triggered Hydrogen-Bond-Breaking Deprotonation Mechanism: Fluorescent Detection of Cyanide Using a Thioacetohydrazone-Functionalized Bispillar [5]arene. *New J. Chem.* **2018**, *42*, 1271–1275. [CrossRef]
29. Wei, T.-B.; Li, W.-T.; Li, Q.; Su, J.-X.; Qu, W.-J.; Lin, Q.; Yao, H.; Zhang, Y.-M. A Turn-On Fluorescent Chemosensor Selectively Detects Cyanide in Pure Water and Food Sample. *Tetrahedron Lett.* **2016**, *57*, 2767–2771. [CrossRef]
30. Ma, J.; Dasgupta, P.K. Recent Developments in Cyanide Detection: A Review. *Anal. Chim. Acta* **2010**, *673*, 117–125. [CrossRef]
31. Rashid, A.; Mondal, S.; Ghosh, P. Development and Application of Ruthenium(II) and Iridium(III) Based Complexes for Anion Sensing. *Molecules* **2023**, *28*, 1231. [CrossRef] [PubMed]
32. Kumar, S.; Singh, S.; Kumar, A.; Murthy, K.S.R.; Singh, A.K. pH-Responsive Luminescence Sensing, Photoredox Catalysis and Photodynamic Applications of Ruthenium(II) Photosensitizers Bearing Imidazo[4,5-f][1,10]phenanthroline Scaffolds. *Coord. Chem. Rev.* **2022**, *452*, 214272. [CrossRef]
33. Therrien, B. Ruthenium-Based Sensors. *Inorganics* **2024**, *12*, 239. [CrossRef]
34. Li, M.-J.; Lin, Z.; Chen, X.; Chen, G. Colorimetric and Luminescent Bifunctional Ru(II) Complexes for Rapid and Highly Sensitive Recognition of Cyanide. *Dalton Trans.* **2014**, *43*, 11745–11751. [CrossRef]
35. Zhu, J.-W.; Ou, H.-D.; Xu, N.; Deng, W.; Yao, Z.-J. Ruthenium-Based Phosphorescent Probe for Selective and Naked-Eye Detection of Cyanide in Aqueous Media. *Dyes Pigm.* **2020**, *176*, 108196. [CrossRef]
36. Mardanya, S.; Karmakar, S.; Bar, M.; Baitalik, S. Pyrene-Biimidazole Based Ru(II) and Os(II) Complexes as Highly Efficient Probes for the Visible and Near-Infrared Detection of Cyanide in Aqueous Media. *Dalton Trans.* **2015**, *44*, 21053–21072. [CrossRef]
37. Alreja, P.; Kaur, N. Establishing the anion recognition correlation of the 2-(2-methoxyphenyl)-1H-imidazo [4, 5-f][1,10] phenanthroline and its $Ru(bipy)_2^{2+}$ complex via fluorimetry. *J. Lumin.* **2016**, *179*, 372–377. [CrossRef]
38. Pal, P.; Ganguly, T.; Karmakar, S.; Baitalik, S. Anion- and solvent induced modulation of photophysical properties of a luminescent bimetallic Ru(II) complex: Experimental and TD-DFT study. *Inorg. Chim. Acta* **2020**, *502*, 119337. [CrossRef]
39. Bar, M.; Maity, D.; Das, K.; Baitalik, S. Asymmetric Bimetallic Ruthenium(II) Complexes Selectively Sense Cyanide in Water through Significant Modulation of Their Ground and Excited State Properties. *Sens. Actuators B* **2017**, *251*, 208–223. [CrossRef]
40. Zavalishin, M.N.; Guschin, A.A.; Nikitin, G.A.; Gamov, G.A. Two Isoniazid-Based Chemosensors for the Detection of Cyanide Ions in Solution: An Experimental and Computational Study. *Photochem. Photobiol. Sci.* **2025**, *24*, 53–63. [CrossRef] [PubMed]
41. Barkale, H.V.; Dey, N. Selective Sensing of Cyanide Ions: Impact of Molecular Design and Assembly on the Response of π-Conjugated Acylhydrazone Compounds. *RSC Adv.* **2024**, *14*, 25108–25114. [CrossRef]
42. Gaumerd, V.; Capello, Y.; Bonnin, Q.; Renard, P.-Y.; Romieu, A. Fluorogenic Detection of Cyanide Ions in Pure Aqueous Media through an Intramolecular Crossed-Benzoin Reaction: Limitations Unveiled and Possible Solutions. *Analyst* **2025**, *150*, 168–176. [CrossRef]
43. Zhao, J.; Zhou, Z.; Li, G.; Stang, P.J.; Yan, X. Light-Emitting Self-Assembled Metallacages. *Natl. Sci. Rev.* **2021**, *8*, nwab045. [CrossRef]
44. Yin, C.; Du, J.; Olenyuk, B.; Stang, P.J.; Sun, Y. The Applications of Metallacycles and Metallacages. *Inorganics* **2023**, *11*, 54. [CrossRef]
45. Tang, J.-H.; Zhong, Y.-W. Anthracene-Containing Metallacycles and Metallacages: Structures, Properties, and Applications. *Inorganics* **2022**, *10*, 88. [CrossRef]
46. Li, Y.; Zhang, J.; Li, H.; Fan, Y.; He, T.; Qiu, H.; Yin, S. Metallacycle/Metallacage-Cored Fluorescent Supramolecular Assemblies with Aggregation-Induced Emission Properties. *Adv. Opt. Mater.* **2020**, *8*, 1902190. [CrossRef]
47. Ludden, M.D.; Ward, M.D. Outside the Box: Quantifying Interactions of Anions with the Exterior Surface of a Cationic Coordination Cage. *Dalton Trans.* **2021**, *50*, 2782–2791. [CrossRef]
48. Yadav, S.; Kannan, P.; Qiu, G. Cavity-Based Applications of Metallo-Supramolecular Coordination Cages (MSCCs). *Org. Chem. Front.* **2020**, *7*, 2842–2872. [CrossRef]
49. Zhang, L.; Liu, H.; Yuan, G.; Han, Y.-F. Chiral Coordination Metallacycles/Metallacages for Enantioselective Recognition and Separation. *Chin. J. Chem.* **2021**, *39*, 2273–2286. [CrossRef]
50. Vardhan, H.; Mehta, A.; Ezugwu, C.I.; Verpoort, F. Self-Assembled Arene Ruthenium Metalla-Assemblies. *Polyhedron* **2016**, *112*, 104–108. [CrossRef]
51. Barry, N.P.E.; Therrien, B. Host–Guest Chemistry in the Hexanuclear (Arene)ruthenium Metalla-Prismatic Cage $[Ru_6(p\text{-cymene})_6(tpt)_2(dhnq)_3]^{6+}$. *Eur. J. Inorg. Chem.* **2009**, *2009*, 4695–4700. [CrossRef]
52. Dhara, S.; Ansari, M.A.; Lahiri, G.K. Host–Guest Feature of DPPP Bridged Arene–Ruthenium Clip Derived Molecular Rectangle. *Inorg. Chem.* **2019**, *58*, 10991–10999. [CrossRef]
53. Maatouk, A.; Rossel, T.; Therrien, B. Allosteric Fluorescent Detection of Saccharides and Biomolecules in Water from a Boronic Acid Functionalized Arene Ruthenium Assembly Hosting Fluorescent Dyes. *Inorganics* **2025**, *13*, 1. [CrossRef]
54. Grzybowski, M.; Gryko, D.T. Diketopyrrolopyrroles: Synthesis, Reactivity, and Optical Properties. *Adv. Opt. Mater.* **2015**, *3*, 280–320. [CrossRef]

55. Mishra, A.; Kang, S.C.; Chi, K.-W. Coordination-Driven Self-Assembly of Arene–Ruthenium Compounds. *Eur. J. Inorg. Chem.* **2013**, *2013*, 5222–5232. [CrossRef]
56. Barare, B.; Babahan, I.; Hijji, Y.M.; Bonyi, E.; Tadesse, S.; Aslan, K. A Highly Selective Sensor for Cyanide in Organic Media and on Solid Surfaces. *Sensors* **2016**, *16*, 271. [CrossRef]
57. Bíró, L.; Hüse, D.; Bényei, A.C.; Buglyó, P. Interaction of $[Ru(\eta^6\text{-p-cym})(H_2O)_3]^{2+}$ with Citrate and Tricarballate Ions in Aqueous Solution; X-ray Crystal Structure of Novel Half-Sandwich Ru(II)-Citrato Complexes. *J. Inorg. Biochem.* **2012**, *116*, 116–125. [CrossRef]
58. Mizuguchi, J.; Wooden, G. A Large Bathochromic Shift from the Solution to the Solid State in 1,4-Diketo-3,6-Diphenyl-Pyrrolo[3,4-c]pyrrole. *Ber. Bunsenges. Phys. Chem.* **1991**, *95*, 1264–1274. [CrossRef]
59. Mataga, N.; Kubota, T. *Molecular Interactions and Electronic Spectra*; Marcel Dekker: New York, NY, USA, 1970.
60. Borah, J.; Hazarika, U.N.; Khakhlary, P. Extending the Chemistry of Reaction between BODIPY and Cyanide Ions: An Application in Selective Sensing of Fluoride and Cyanide Ions. *ACS Omega* **2022**, *7*, 46234–46240. [CrossRef]
61. Ho, J.; Coote, M.L. A universal approach for continuum solvent pK_a calculations: Are we there yet? *Theor. Chem. Acc.* **2010**, *125*, 3–21. [CrossRef]
62. ChemAxon Software. *Calculators Playground*, v.1.6.2. ChemAxon. Available online: http://www.chemaxon.com (accessed on 25 September 2025).
63. Adamo, C.; Scuseria, G.E.; Barone, V. Accurate excitation energies from time-dependent density functional theory: Assessing the PBE0 model. *J. Chem. Phys.* **1999**, *111*, 2889–2899. [CrossRef]
64. Palakkeezhillam, V.N.V.; Haribabu, J.; Kumar, V.S.; Santibanez, J.F.; Manakkadan, V.; Rasin, P.; Garg, M.; Bhuvanesh, N.; Sreekanth, A. Unraveling the anticancer efficacy and biomolecular properties of Ru(II)-arene complexes of pyrene-based thiosemicarbazone ligands: A comprehensive In silico/In vitro exploration. *Organometallics* **2024**, *43*, 242–260. [CrossRef]
65. Abirami, A.; Devan, U.; Ramesh, R.; Velanganni, A.A.J.; Małecki. Naphthoyl benzhydrazine–decorated binuclear arene Ru(II) complexes as anticancer agents targeting human breast cancer cells. *Dalton Trans.* **2023**, *52*, 16376–16387. [CrossRef]
66. Fonseca Guerra, C.; Handgraaf, J.W.; Baerends, E.J.; Bickelhaupt, F.M. Voronoi Deformation Density (VDD) Charges: Assessment of the Mulliken, Bader, Hirshfeld, Weinhold, and VDD Methods for Charge Analysis. *J. Comput. Chem.* **2004**, *25*, 189–210. [CrossRef]
67. Hirshfeld, F.L. Bonded-Atom Fragments for Describing Molecular Charge Densities. *Theor. Chim. Acta* **1977**, *44*, 129–138. [CrossRef]
68. Li, G.; Tao, F.; Wang, H.; Wang, L.; Zhang, J.; Ge, P.; Liu, L.; Tong, Y.; Sun, S. A Novel Reversible Colorimetric Chemosensor for the Detection of Cu^{2+} Based on a Water-Soluble Polymer Containing Rhodamine Receptor Pendants. *RSC Adv.* **2015**, *5*, 18983–18989. [CrossRef]
69. Shiraishi, Y.; Yamamoto, K.; Sumiya, S.; Hirai, T. Spiropyran as a Reusable Chemosensor for Selective Colorimetric Detection of Aromatic Thiols. *Phys. Chem. Chem. Phys.* **2014**, *16*, 12137–12142. [CrossRef]
70. DeGroot, H.P.; Hanusa, T.P. Cyanide Complexes of the Transition Metals. In *Encyclopedia of Inorganic and Bioinorganic Chemistry*; King, R.B., Ed.; Wiley: Chichester, UK, 2020.
71. Beck, M.T. Critical Survey of Stability Constants of Cyano Complexes. *Pure Appl. Chem.* **1987**, *59*, 1703–1720. [CrossRef]
72. Gholami, M.D.; Liu, Q.; Sonar, P.; Manzhos, S.; Ayoko, G.A.; Izake, E.L. Naphthalene flanked diketopyrrolopyrrole: A new functional dye based optical sensors for monitoring cyanide ions in water. *Adv. Mater. Technol.* **2022**, *7*, 2100170. [CrossRef]
73. Lv, X.; Liu, J.; Liu, Y.L.; Zhao, Y.; Chen, M.; Wang, P.; Guo, W. Rhodafluor-Based Chromo- and Fluorogenic Probe for Cyanide Anion. *Sens. Actuators B Chem.* **2011**, *158*, 405–410. [CrossRef]
74. Garci, A.; Dobrov, A.A.; Riedel, T.; Orhan, E.; Dyson, P.J.; Arion, V.B.; Therrien, B. Strategy to Optimize the Biological Activity of Arene Ruthenium Metalla-Assemblies. *Organometallics* **2014**, *33*, 3813–3822. [CrossRef]
75. Jenni, S.; Ponsot, F.; Baroux, P.; Collard, L.; Ikeno, T.; Hanaoka, K.; Quesneau, V.; Renault, K.; Romieu, A. Design, Synthesis and Evaluation of Enzyme-Responsive Fluorogenic Probes Based on Pyridine-Flanked Diketopyrrolopyrrole Dyes. *Spectrochim. Acta Part A* **2021**, *248*, 119179. [CrossRef]
76. Romero, R.; Salgado, P.R.; Soto, C.; Contreras, D.; Melin, V. An Experimental Validated Computational Method for pKa Determination of Substituted 1,2-Dihydroxybenzenes. *Front. Chem.* **2018**, *6*, 208. [CrossRef]
77. Salgado, L.E.V.; Vargas-Hernández, C. Spectrophotometric Determination of the pK_a, Isosbestic Point, and Equation of Absorbance vs. pH for a Universal pH Indicator. *Am. J. Anal. Chem.* **2014**, *5*, 1290–1301. [CrossRef]
78. Czyrski, A. The Spectrophotometric Determination of Lipophilicity and Dissociation Constants of Ciprofloxacin and Levofloxacin. *Spectrochim. Acta A Mol. Biomol. Spectrosc.* **2022**, *265*, 120343. [CrossRef]
79. Gran, G. Determination of the Equivalence Point in Potentiometric Titrations. *Acta Chem. Scand.* **1950**, *4*, 559–577. [CrossRef]
80. Te Velde, G.; Bickelhaupt, F.M.; Baerends, E.J.; Fonseca Guerra, C.; van Gisbergen, S.J.A.; Snijders, J.G.; Ziegler, T. Chemistry with ADF. *J. Comp. Chem.* **2021**, *22*, 931. [CrossRef]

81. Fonseca Guerra, C.; Snijders, J.G.; te Velde, G.; Baerends, E.J. Towards an order-N DFT method. *Theor. Chem. Acc.* **1998**, *99*, 391. [CrossRef]
82. Baerends, E.J.; Ziegler, T.; Autschbach, J.; Bashford, D.; Bérces, A.; Bickelhaupt, F.M.; Bo, C.; Boerrigter, P.M.; Cavallo, L.; Chong, D.P.; et al. ADF2014, SCM, Theoretical Chemistry, Vrije Universiteit, Amsterdam, The Netherlands. Available online: https://www.scm.com/amsterdam-modeling-suite/adf/ (accessed on 25 September 2025).
83. Chong, D.P. Augmenting basis set for time-dependent density functional theory calculation of excitation energies: Slater-type orbitals for hydrogen to krypton. *Mol. Phys.* **2005**, *103*, 749. [CrossRef]
84. Klamt, A.; Schürmann, G.J. COSMO: A new approach to dielectric screening in solvents with explicit expressions for the screening energy and its gradient. *J. Chem. Soc. Perkin Trans.* **1993**, *2*, 799. [CrossRef]
85. Klamt, A.; Jonas, V. Treatment of the outlying charge in continuum solvation models. *J. Chem. Phys.* **1996**, *105*, 9972. [CrossRef]
86. Pye, C.C.; Ziegler, T. An implementation of the conductor-like screening model of solvation within the Amsterdam density functional package. *Theor. Chem. Acc.* **1999**, *101*, 396. [CrossRef]
87. Microsoft Corporation. *Microsoft Excel, Version 2016*; Microsoft Corporation: Redmond, WA, USA, 2016.
88. GraphPad Software. *GraphPad Prism*, Version 5.0; GraphPad Software Inc.: San Diego, CA, USA, 2008.
89. Analytical Methods Committee. Recommendations for the Definition, Estimation and Use of the Detection Limit. *Analyst* **1987**, *112*, 199–204. [CrossRef]
90. Schneider, H.-J.; Yatsimirsky, A. *Principles and Methods in Supramolecular Chemistry*; John Wiley & Sons: Chichester, UK, 2000; p. 142.
91. Rumble, J.R. (Ed.) *CRC Handbook of Chemistry and Physics*, 105th ed.; CRC Press: Boca Raton, FL, USA, 2024.